Acta Pharmaceutica Sinica B 2023;13(1):298–314

Chinese Pharmaceutical Association
Institute of Materia Medica, Chinese Academy of Medical Sciences

Acta Pharmaceutica Sinica B

www.elsevier.com/locate/apsb
www.sciencedirect.com

ORIGINAL ARTICLE

A neutrophil-biomimic platform for eradicating metastatic breast cancer stem-like cells by redox microenvironment modulation and hypoxia-triggered differentiation therapy

Yongchao Chu, Yifan Luo, Boyu Su, Chao Li, Qin Guo, Yiwen Zhang, Peixin Liu, Hongyi Chen, Zhenhao Zhao, Zheng Zhou, Yu Wang, Chen Jiang*, Tao Sun*

Key Laboratory of Smart Drug Delivery (Ministry of Education), Minhang Hospital, State Key Laboratory of Medical Neurobiology and MOE Frontiers Center for Brain Science, Department of Pharmaceutics, School of Pharmacy, Research Center on Aging and Medicine, Fudan University, Shanghai 201203, China

Received 21 February 2022; received in revised form 10 April 2022; accepted 15 May 2022

KEY WORDS

Metastasis;
Breast cancer;
Neutrophil;
Hypoxia;
Cancer stem cell;
Glutathione;
Reactive oxygen species;
Nitroimidazole

Abstract Metastasis accounts for 90% of breast cancer deaths, where the lethality could be attributed to the poor drug accumulation at the metastatic loci. The tolerance to chemotherapy induced by breast cancer stem cells (BCSCs) and their particular redox microenvironment further aggravate the therapeutic dilemma. To be specific, therapy-resistant BCSCs can differentiate into heterogeneous tumor cells constantly, and simultaneously dynamic maintenance of redox homeostasis promote tumor cells to retro-differentiate into stem-like state in response to cytotoxic chemotherapy. Herein, we develop a specifically-designed biomimic platform employing neutrophil membrane as shell to inherit a neutrophil-like tumor-targeting capability, and anchored chemotherapeutic and BCSCs-differentiating reagents with nitroimidazole (NI) to yield two hypoxia-responsive prodrugs, which could be encapsulated into a polymeric nitroimidazole core. The platform can actively target the lung metastasis sites of triple negative breast cancer (TNBC), and release the escorted drugs upon being triggered by the hypoxia microenvironment. During the responsiveness, the differentiating agent could promote transferring BCSCs into non-BCSCs, and simultaneously the nitroimidazole moieties conjugated on the polymer and prodrugs could modulate the tumor microenvironment by depleting nicotinamide adenine dinucleotide phosphate hydrogen (NADPH) and amplifying intracellular oxidative stress to prevent tumor cells retro-differentiation into BCSCs. In combination, the BCSCs differentiation and tumor microenvironment

*Corresponding author. Tel./fax: +86 21 5198 0079.
E-mail addresses: jiangchen@shmu.edu.cn (Chen Jiang), sunt@fudan.edu.cn (Tao Sun).

Peer review under responsibility of Chinese Pharmaceutical Association and Institute of Materia Medica, Chinese Academy of Medical Sciences.

https://doi.org/10.1016/j.apsb.2022.05.027

modulation synergistically could enhance the chemotherapeutic cytotoxicity, and remarkably suppress tumor growth and lung metastasis. Hopefully, this work can provide a new insight in to comprehensively treat TNBC and lung metastasis using a versatile platform.

1. Introduction

Metastasis accounts for 90% of breast cancer deaths[1]. TNBC is the most aggressive and metastatic subtype of breast cancer and has become a serious clinical conundrum due to its frequent recurrence and distal metastasis[2]. Approximately 60% of breast cancer patients suffer from lung metastasis[3]. Despite recent advances in surgery and radiotherapy, chemotherapy remains the preferred treatment for metastatic TNBC patients[4]. Unfortunately, these strategies do not effectively increase the survival rate of patients due to the poor drug accumulation at the metastatic loci and tumor tolerance to chemotherapy[5–7]. Hence, developing an effective strategy with improving drug concentration in metastatic lesion and chemosensetivity of tumor cells is of utmost importance for enhancing anti-metastasis therapy of TNBC.

To elevate the drug accumulation at tumor sites, several nanosystems have been designed to deliver chemotherapeutic reagents into the tumor relying on the size effects of tumor[8]. However, it should be clearly noted that the size effect is primarily confined to vascularized solid tumors with diameters larger than ~4.6 mm[9]. Nevertheless, the metastatic foci are small clusters of cancer cells with poor vasculature and angiogenic dormancy, which severely hinders the access of nanosystems delivery[10]. Hence, the active chemotactic delivery systems need to be developed urgently to enhance the drug capacity of targeting and enrichment in metastatic lesion.

In the progression of TNBC metastasis, inflammatory cells, represented by neutrophils, play crucial roles[11]. Prior to cancer metastasis, neutrophils are preferentially recruited to the pre-metastatic niche to produce leukotriene B4 (LTB4) and matrix metalloproteinase 9 (MMP9), which can create an inflammatory environment to provide a suitable "soil" for tumor cells[12]. The inflammatory microenvironment, correspondingly, would further amplify more neutrophil recruitment. Simultaneously, these recruited neutrophils can release neutrophil extracellular traps (NETs) to facilitate the colonization of cancer cells at metastasis sites[13]. During the formation of metastasis foci, tumor cells and the surrounding microenvironment continue to produce signals, including chemokines (such as CXCR2), cytokines (such as TNF-α, IL-17) and hydrogen peroxide, to actively recruit neutrophils[12,14]. Hence, neutrophils remain in active phase during the overall progression of the tumor metastasis and possess naturally targeting chemotaxis tendency to metastasis foci. Neutrophils and their derivates could thus serve as drug vehicles for tumoral metastasis delivery[15,16].

Breast cancer stem cells (BCSCs) and special redox microenvironment are believed to be significant contribution to the chemotherapy resistance of metastatic TNBC[17,18]. BCSCs are innately resistant to cytotoxic agents, and remain dormant at metastatic sites until conditions that are conducive to their proliferation and differentiation[19–21]. It has been found that dynamic maintenance of redox homeostasis promotes tumor cells to retro-differentiate into stem-like state in response to cytotoxic chemotherapy[22,23]. Currently, differentiation therapy is a conventional treatment approach against cancer stem cells (CSCs), among which, differentiating reagents (such as all-trans retinoic acid, ATRA) can coax malignant cells to differentiate into less stem-like undifferentiated phenotypes[24–28]. However, single differentiation therapy suffers from non-shrinking solid tumor size and even carries the risk that induces dormant BCSCs in metastatic sites to enter a proliferative state, which attributes to that adaptive antioxidant systems of tumor cells in redox microenvironment can promote them to turn into CSCs constantly[29]. Our previous study found that disturbing the intratumoral glutathione (GSH)-reactive oxygen species (ROS) balance can promote tumor cell apoptosis[30]. Therefore, it might be a more reliable strategy for increasing the chemotherapy sensitivity by promoting BCSCs differentiation and simultaneously modulating the redox microenvironment for preventing non-BCSCs retro-differentiation.

The nicotinamide adenine dinucleotide phosphate hydrogen (NADPH) is a key component to maintain the intracellular redox balance, which donates electrons and aids the reduction of oxidized glutathione (GSSG) to GSH by glutathione reductase (GR). Numerous studies elucidated that in hypoxic tumor microenvironment, the overexpressed nitroreductase and NAD(P)H quinone dehydrogenase 1 (NQO1) act as a substrate for some hypoxia-activated moieties, such as nitroaromatics, which provide a potential opportunity for selectively depleting NADPH[31,32]. Therefore, drug delivery system based on the nitroreductase exhibit great potential in breaking intracellular redox balance to prevent tumor cells retro-differentiation into CSCs.

To overcome the obstacles to metastatic breast cancer therapy, in this work, we developed a specifically-designed biomimic platform employing neutrophil membrane as shell to inherit a neutrophil-like tumor-targeting capability and anchored chemotherapeutic doxorubicin (DOX) and BCSCs-differentiating ATRA with nitroimidazole to yield two hypoxia-responsive prodrugs, which could be encapsulated into a polymeric nitroimidazole core assembled from a nitroaromatics-derived block polymer (Scheme 1). It was postulated that neutrophil-motivated platforms can actively target the lung macrometastasis and micrometastasis of TNBC, and release the escorted drugs upon being triggered by the hypoxia microenvironment at metastatic sites. During the responsiveness, ATRA could differentiate BCSCs into non-BCSCs, and simultaneously the nitroimidazole moieties on the polymer and prodrugs could modulate the tumor microenvironment by depleting NADPH to break intracellular redox balance and further prevent tumor cells retro-differentiation into BCSCs. In combination, the BCSCs differentiation and tumor microenvironment modulation synergistically could enhanced chemotherapeutic cytotoxicity and eventually satisfies the demand for facilitating a maximized synergistic anti-metastasis efficacy.

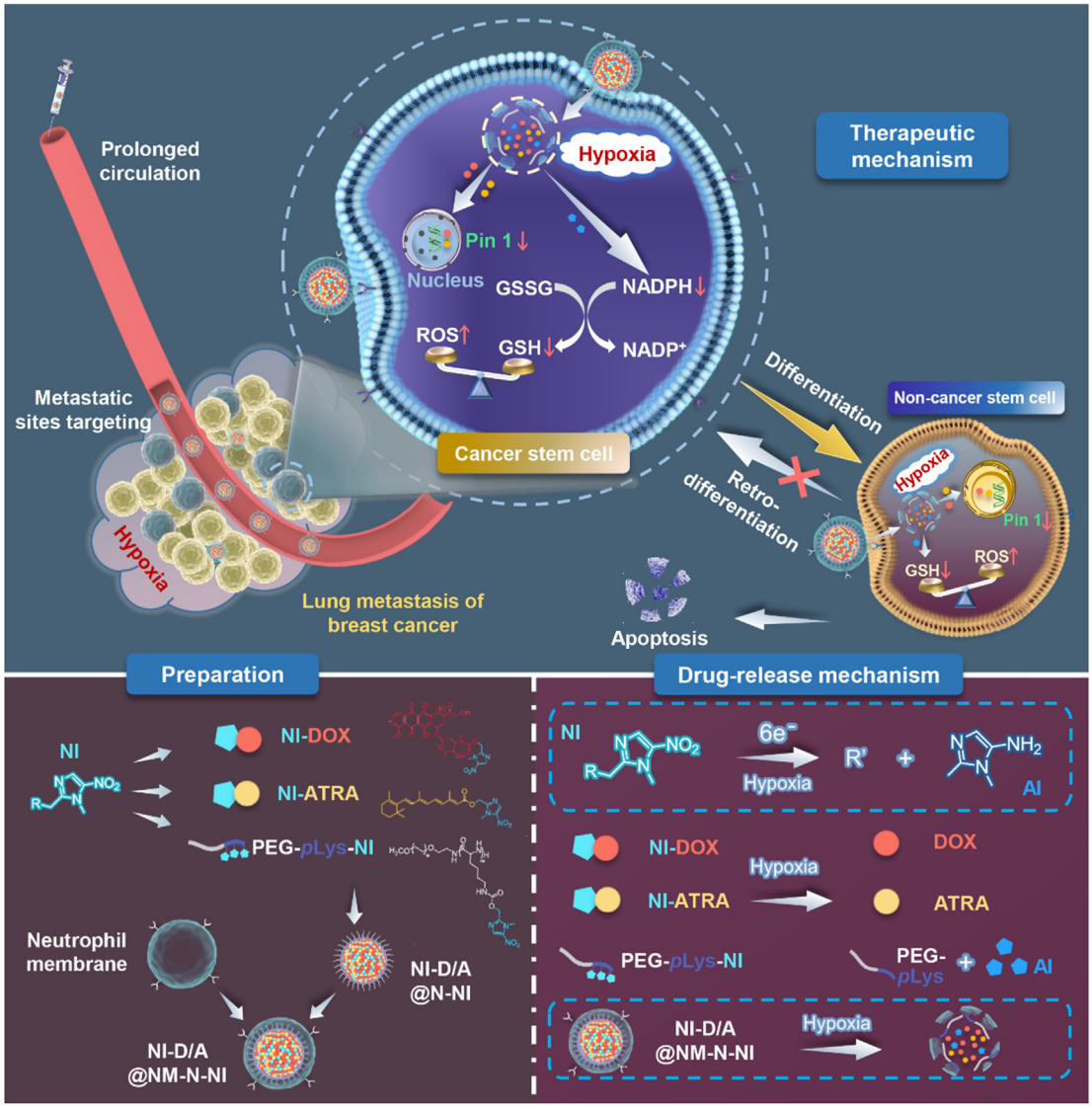

Scheme 1 Schematic illustration of neutrophil-biomimic platform for eradicating metastatic breast cancer stem-like cells by redox microenvironment modulation and hypoxia-triggered differentiation therapy.

2. Materials and methods

2.1. *Materials, cell lines and animals*

Methoxypolyethylene glycol amine (mPEG-NH_2, Mw = 5000) were purchased from Jenkem technology Co., Ltd. (Beijing, China). DOX, ATRA, Did, coumarin-6 and TUNEL Apoptosis Assay Kit were supplied by Meilune Biological technology Co., Ltd. (Dalian, China). Dulbecco's modified Eagle's medium (DMEM, high glucose) and FBS were supplied by Gibco BRL (Carlsbad, CA, USA). Hoechst 33,342 were purchased from Thermo Fisher Scientific Co., Ltd. (Shanghai, China). Anti-CD11b (ab133357), Anti-CD44 antibody (ab189524), Goat Anti-Rabbit IgG H&L Alexa Fluor 594 (ab150080) and Goat Anti-Mouse IgG H&L Alexa Fluor 488 (ab150117) were purchased from Abcam Inc. (Cambridge, MA, UK). Mouse Pin 1 antibody was purchased from R&D systems, Inc. (Minneapolis, Minnesota, USA). Anti-ALDH1A1 antibody (A01392) was purchased from Boster Biological Technology Co., Ltd. (Wuhan, China). CXCR4 rabbit pAb (A1303) was purchased from ABclonal Technology Co., Ltd. (Wuhan, China). A phosphatase and protease inhibitor cocktail (P1050), Enhanced BCA Protein Assay Kit (P0010), $NADP^+$/NADPH Assay Kit with WST-8 (S0179), Cell lysis buffer for western and Coomassie blue fast staining solution were purchased from Beyotime Biotechnology Co., Ltd. (Shanghai, China). GSH assay kit was purchased from Jiancheng Bioengineering Institute (Nanjing, China). All other chemicals were provided by Sinopharm Chemical Reagent Co., Ltd. (Shanghai, China) unless mentioned otherwise.

4T1, luciferase-expressing 4T1 (4T1-Luc) cells and ERFP-expressing 4T1 (4T1-ERFP) cells were purchased from Stem Cell Bank, Chinese Academy of Sciences (Shanghai, China). 4T1 cells were cultured in RPMI-1640 medium supplemented with 10% fetal bovine serum and 1% antibiotics (penicillin and streptomycin) at 37 °C under the air atmosphere of 5% CO_2. All experiments were performed on cells in the logarithmic growth phase.

4T1 BCSCs were obtained from ordinary 4T1 cells with the ALDEFLUOR assay according to the manufacturer's instruction

(STEMCELL Technologies, Vancouver, Canada) and were cultured in a DMEM/F12 medium supplemented with 10 ng/mL bFGF, 20 ng/mL EGF, 1 ng/mL insulin, 2% B-27 and 1% antibiotics at 37 °C under the air atmosphere of 5% CO_2.

ICR and BALB/c female mice (6−8 weeks, 18−22 g, SPF) were purchased from Slac Laboratory Animal Co., Ltd. (Shanghai, China). All of our animal experiments were managed in conformity with guidelines evaluated and approved by Fudan University Institutional Animal Care and Use Committee (IACUC).

2.2. Isolation of the neutrophil membrane

The neutrophils were isolated from the femur and humerus of ICR mouse by a percoll gradient method as previously described[33]. The obtained neutrophils were activated after incubation in serum-free RPMI 1640 medium with recombinant mouse tumor necrosis factor-α (TNF-α) for 2 h at 37 °C. To isolate activated neutrophils membrane, the collected neutrophils were suspended in the hypotonic lysing buffer-1 containing 30 mmol/L Tris-HCl (pH 7.2), 225 mmol/L D-mannitol, 75 mmol/L sucrose, 0.2 mmol/L EDTA and a phosphatase and protease inhibitor cocktail. Thereafter, they were homogenized and centrifuged at 3500 rpm for 10 min at 4 °C to remove the intact cells and nuclei. The supernatant was then centrifuged at 14,000 rpm (Thermo Sorvall ST16R, Thermo Fisher Scientific, Waltham, MA, USA) at 4 °C to eliminate the mitochondria. The supernatant was centrifuged for a second time at 100,000×*g* (HITACHI CP100NK, Tokyo, Japan) for 1 h to extract neutrophils membrane. Membrane content was quantified by BCA Protein Assay Kit.

2.3. Preparation and characterizations of NM-N-NI

Preparation of the NI-modified nanocore (N-NI): The nanocore encapsulated with NI-DOX and NI-ATRA (NI-D/A@N-NI) was prepared by a film hydration method[34]. Briefly, 40 mg of NI-modified polyethylene glycol-polylysine (PEG-*p*Lys-NI) dissolved in 2 mL of *N*,*N*-dimethylformamide (DMF), was mixed with NI-modified ATRA (NI-ATRA) and NI-modified DOX (NI-DOX). The DMF was removed under rotary evaporation by oil pump and the obtained thid film was hydrated by 50 mL of phosphate buffer saline (PBS) for 2 h with light protection. Finally, N-NI was obtained after filtration through a 0.45 μm membrane to remove the non-encapsulated drugs. The quantification of NI-ATRA and NI-DOX was detected by high performance liquid chromatography (HPLC) system (Shimadzu LC-20AD, Kyoto, Japan). For the *in vitro* and *in vivo* experiments, pyrene, coumarin-6 and Did were encapsulated in the nanocore with the same procedure, respectively. The critical micelle concentration (CMC) of PEG-*p*Lys-NI were estimated using pyrene as the fluorescent probe.

Preparation of N-NI coated with NM (NM-N-NI): NM-N-NI was fabricated with a neutrophil membrane by a direct extrusion method. Briefly, the 0.2 mg/mL of neutrophil membrane was mixed with the nanocore N-NI with a PEG-*p*Lys-NI concentration of 1.0 mg/mL and sequentially extruded through a 400 and 200 nm porous polycarbonate membrane to form NM-N-NI. The particles diameter and surface charge were determined by the dynamic light scattering (DLS) technique using (Zetasizer Nano ZS, Malvern, UK). The morphological analysis was carried out using transmission electron microscope (TEM), (HITACHI HT7700, Tokyo, Japan). The NI-ATRA and NI-DOX loadings in NM-N-NI (NI-D/A@NM-N-NI) were analyzed by the HPLC and fluorescence spectrophotometers method, respectively.

Protein detection in NM-N-NI: The membrane-associated protein on prehomogenated neutrophils, neutrophil membrane vesicles (NMV), and NM-N-NI were characterized by Coomassie blue staining. The protein components were extracted with a RIPA lysis buffer containing protease inhibitor, and the protein concentration of samples was quantified by enhanced BCA kit. Then, 20 μg of protein from each sample was separated by 10% Tris/glycine SDS-polyacrylamide gelatin. For the total imaging, the protein blots were stained with Coomassie blue fast staining solution, and analyzed by Image Lab software (Bio-Rad, Hercules, CA, USA).

Furthermore, after electrophoresis, the proteins were transferred onto polyvinylidene fluoride (PVDF) membrane, which then blocked with non-fat skimmed milk (5%) and incubated with anti-CXCR4 (1:1000), anti-CD11b (1:1000) and anti-Tublin (1:2000) overnight at 4 °C. Next, the membrane was incubated with horseradish peroxidase (HRP)-conjugated secondary antibody (1:1000) for 2 h, and followed by detection with electrochemiluminescent HRP substrate and analyzed with Image Lab software (Bio-Rad).

2.4. In vitro drug release evaluation

To characterize the structural conversion from the NI to AI (aminoimidazole) group under the hypoxic condition, NI-D/A@N-NI was dispersed in PBS and incubated in a shake at 37 °C under normoxic conditions or simulated hypoxic conditions with $Na_2S_2O_4$ (20 mmol/L). The absorbance spectra of NI-DOX, NI-ATRA and PEG-*p*Lys-NI were scanned using an ultraviolet spectrophotometer (EU-2600 A, Onlab, Shanghai, China).

To evaluate the drug release of NM-N-NI, the fluorescent pyrene was used as the probe and a simulated hypoxic condition was established with 100 μmol/L NADPH and 2 mg/mL liver microsomes that were added into the degassed PBS at 37 °C. The hypoxic environment was maintained by degassing oxygen with nitrogen. The quantities of pyrene in the release medium were determined using fluorospectro photometer (RF-5301PC, SHIMADZU, Kyoto, Japan).

2.5. Cellular uptake and internalization mechanism

Cellular uptake: 4T1 cells were separately seeded into 24-well plate at a density of 1.0×10^4 cells per well. Upon achieving a 70% cell density, the cells were maintained under hypoxic condition for 6 h. Then the medium was replaced with coumarin 6-labeled N-NI (Coumarin-6@N-NI) or coumarin 6-labeled NM-N-NI (Coumarin-6@NM-N-NI) at a concentration of 50 ng/mL coumarin-6. After different time incubation, cells were washed with PBS and then visualized under the inverted fluorescence microscope (710 META, Zeiss, Jena, Germany). Further, flow cytometry analysis was used to evaluate the cellular uptake of different formulations.

Internalization mechanism: To analyze the possible internalization mechanism, 4T1 cells were seeded in 24-well culture plates. Upon achieving a 70% cell density, the cells were maintained under hypoxic condition for 6 h. Then the cells were incubated with coumarin-6@N-NI or coumarin-6@NM-N-NI (coumarin-6 concentration: 30 ng/mL) for another 30 min. Other groups were incubated with the same coumarin-6-encapsulated formulations as well as different inhibitors including filipin

(0.5 μg/mL), chlorpromazine (0.4 μg/mL), and wortmannin (1 μg/mL). After incubation for 30 min, the cells were digested by trypsin−EDTA, collected by centrifugation and resuspended in PBS. Then the cellular fluorescence was detected by flow cytometer (cytoFLEX, Beckman Coulter, Brea, CA, USA).

4T1 cells were seeded in a glass bottom dish, allowed to adhere for 24 h under standard conditions and then maintained under hypoxic condition for 6 h. Upon reaching a 70% cell density, the cells were maintained under hypoxic condition for 6 h. After incubation with coumarin-6@NM-N-NI for 0.5 and 2 h, lysotracker red (Thermo Fisher Scientific, Waltham, MA, USA) was added and dyed for 20 min. Afterwards, cells were washed with PBS, stained with DAPI, and visualized by the confocal laser scanning microscopy (CLSM, 710 META, Zeiss, Jena, Germany).

2.6. Cell apoptosis assays and cellular toxicity

Cell apoptosis assays: To further explore the cell death mechanism induced by various treatments, cell apoptosis assays were carried out. To be specific, 4T1 cells after respective treatments (PBS, free NI-D/A, NI-D/A@N, NI-D/A@N-NI, NI-D/A@NM-N-NI) for 24 h under hypoxic condition. Then cells were collected, washed 3 times with PBS, treated with annexin V-PE/7-AAD apoptosis detection kit (Meilunbio, Dalian, China), and finally detected by the flow cytometer.

Cellular toxicity: The cytotoxicity of different formulation was measured by the standard CCK-8 assay. Briefly, 4T1 cells were inoculated to 96-well plates at a density of 5×10^3/well. After 24 h under standard conditions, the cells were treated with five formulations individually, including free NI-ATRA, free NI-DOX, free NI-D/A, NI-D/A@N-NI, NI-D/A@NM-N-NI, and followed by an additional incubation for 24 h under standard or hypoxic conditions. Finally, the cytotoxicity was accessed by CCK-8 assay. The combination index (CI) of NI-DOX and NI-ATRA combined in NM-N-NI was quantified according to the following Eq. (1):

$$\mathrm{CI} = D_1/D_{\mathrm{m1}} + D_2/D_{\mathrm{m2}} \quad (1)$$

where D_1 and D_2 are the IC_{50} values of NI-DOX and NI-ATRA in dual drug formulations, and D_{m1} and D_{m2} are IC_{50} values of NI-DOX and NI-ATRA in single drug formulations, respectively. The CI lower than one indicates synergism, CI equal to one indicates additive effects, and CI values higher than one indicates antagonism.

2.7. NADPH depletion and redox imbalance

4T1 cells were inoculated into 12-well plates at a density of 7×10^4 cells/well and cultured for 24 h. Then the cells were incubated with PBS, free NI-D/A, NI-D/A@N, NI-D/A@N-NI and NI-D/A@NM-N-NI and followed by additional incubation for 4 h under the standard and hypoxia conditions, respectively. The cells subjected to no treatment were defined as "0 h". Afterward, the cells were washed with PBS and collected by centrifugation at 1500 rpm for 5 min. $NADP^+$/NADPH ratio was determined using the $NADP^+$/NADPH assay kit and the GSH quantification was analysed using the GSH assay kit. The total proteins were quantified using the BCA protein assay kit. Moreover, intracellular ROS level was detected using 2′,7′-dichlorofluorescein diacetate (DCFH-DA), which could be oxidized to produce fluorescent compound of dichlorofluorescein (DCF) in the presence of ROS.

2.8. In vivo metastasis targeting and biodistribution

The lung metastatic cancer mice model received an injection of 4×10^5/mL 4T1-luci cells *via* the tail vein. 7 days post of injection, different formulation (free Did, Did-labeled nanocore assembled with PEG-pLys-NCA (Did@N), Did-labeled N-NI (Did@N-NI), Did-labeled NM-N-NI (Did@NM-N-NI)) were respectively given to the lung metastasis mice at 1 mg/kg of Did by tail vein injections. The signal of Did were monitored by the IVIS Spectrum imaging system (PerkinElmer, Waltham, MA, USA) at 1, 4, 8 and 24 h after administration. The mice were autopsied, and major organs were carefully collected and were homogenized in 1 mL methanol and centrifugated. The supernatant was collected to test the Did concentration by microplate reader (Multiskan MK3, Thermo Scientific, Waltham, MA, USA). Moreover, the orthotopic tumor model was generated by subcutaneous injection of 4T1 cells (2×10^5/mL), 14 days post of injection, different formulations were respectively given to mice and detected by IVIS according to the above method.

The 4T1-ERFP cells were injected into mice at 4×10^5 cells/mouse *via* tail vein to prepare a lung metastasis cancer model. The mice were imaged under the IVIS Spectrum imaging system (PerkinElmer) to determine the formation of lung metastases. Seven days post of the injection, different formulation (free coumarin-6, coumarin-6@N, coumarin-6@N-NI, coumarin-6@NM-N-NI) were respectively given to the lung metastasis model at 1 mg/kg of Did *via* the tail vein injection. Mice were sacrificed after 24 h, and lung were excised and fixed in 4% paraformaldehyde. The tissue sections embedded in optimal cutting temperature (OCT) compound and were visualized under the confocal fluorescence microscope (CLSM, 710 META, Zeiss, Jena, Germany).

2.9. In vivo antitumor efficacy

The orthotopic tumor model was generated by subcutaneous injection of 4T1 cells (2×10^5) diluted in Hank's into the mammary fat pads of BALB/c female mice. At the 14th day after tumor model construction, TNBC bearing mice were divided into nine groups ($n = 10$ per group) randomly according to the tumor size. Different formulations (saline, free D/A, N-NI, free NI-D/A, NI-D/A@N, NI-D@N-NI, NI-A@N-NI, NI-D/A@N-NI, NI-D/A@NM-N-NI) were administered on Days 13, 16, 19, 22, 25, 28 and 31 with NI-ATRA and NI-DOX at concentrations of 3.0 and 1.0 mg/kg, respectively. Tumor sizes and body weight were recorded by caliper every other day from Day 14 to Day 32. The tumor volume was calculated as length × $\mathrm{width}^2/2$.

The mice were sacrificed on Day 35 and the major organs and tumor of mice were excised. The proportion of BCSCs in tumor was assayed by flow cytometry assay. Histological changes in lung and tumor were visualized *via* hematoxylin and eosin (HE) staining. One part of tumors were stored in a refrigerator at −80 °C for frozen sectioning, immunofluorescence analysis, Western blot, and transferase-mediated deoxyuridine triphosphate-biotin nick end labeling (TUNEL) assay (Meilunbio, Dalian, China).

2.10. Analysis of the proportion of BCSCs

The tumors were collected from orthotopic tumor mice model and cut into small pieces, which were digested with 1 mg/mL collagenase Type I solution (Invitrogen, Carlsbad, CA, USA) and

incubated at 37 °C for 2 h. Afterwards, tumor cells were filtered by a 70 μm membrane filter and collected by centrifugation at 1500 rpm for 5 min, and then stained with the ALDEFLUOR assay (STEMCELL Technologies) for flow cytometer analyses.

2.11. Western blot

Immunoblotting was selected to assess the expression of Pin1 and ALDH1 proteins. 4T1 cells were seeded in a 6-well plate and incubated with different formulations (PBS, free NI-D/A, NI-D/A@N, NI-D/A@N-NI, NI-D/A@NM-N-NI) for 24 h. The protein was harvested from cells using lysis buffer for western and the protein concentration was quantified with BCA kit.

To measure the expression of Pin 1 and ALDH1 in the tumor, the tumor tissues were lysed with lysis buffer for western. 20 μg of proteins of each sample were separated by 10% Tris/glycine SDS-polyacrylamide gelatin for the detection of Pin1 and ALDH1 related proteins. The proteins were transferred onto polyvinylidene fluoride (PVDF) membrane, which then blocked with non-fat skimmed milk (5%) and incubated with anti-Pin1 (1:1000), anti-ALDH1A1 (1:1000) and anti-GADPH (1:2000) overnight at 4 °C. Next, the membrane was incubated with horseradish peroxidase (HRP)-conjugated secondary antibody (1:1000) for 2 h, and followed by detection with electrochemiluminescent HRP substrate and analyzed with Image Lab software (Bio-Rad).

2.12. In vivo anti-metastatic efficacy

The *in vivo* anti-metastatic efficacy of NI-D/A@NM-N-NI was evaluated in lung metastatic breast cancer models. The animals were randomly divided into five groups ($n = 10$), and respectively injected with 2×10^5 of 4T1-luci cells *via* tail vein to induce the lung metastatic model. Different formulations (saline, free D/A, N-NI, free NI-D/A, NI-D/A@N, NI-D@N-NI, NI-A@N-NI, NI-D/A@N-NI, NI-D/A@NM-N-NI) were administered on Days 7, 9, 11 and 13 with NI-ATRA and NI-DOX at concentrations of 3.0 and 1.0 mg/kg, respectively. The mice weight and survival data were respectively recorded.

Half of the mice were sacrificed on Day 14 and the lung tissues were carefully removed, photographed and stained with India ink to count the surface metastatic nodules, and further evaluate the inhibition rate of lung metastasis, which was defined as the mean number of lung metastasis from each group compared to that of the saline group. Moreover, the lung tissues from each group were assessed by histological examinations and then stored in a refrigerator at −80 °C for frozen sectioning, immunofluorescence analysis and western blot. The apoptotic cells in lung nodules were assessed by the TUNEL assay (Meilunbio, Dalian, China) according to the commercial instructions.

2.13. Safety evaluation

For the safety evaluation, lung metastatic mice were sacrificed after being treated for 14 days. The blood was obtained to evaluate the level of alanine transaminase (ALT), aspartate transaminase (AST), blood urea nitrogen (BUN) and creatinine (CRE) and the hematoxylin and eosin staining was performed on the main organs sections and visualized with a light microscope.

2.14. Statistical analysis

Results were analyzed by GraphPad Prism 2.0 software (GraphPad Software, San Diego, CA, USA) and presented as means ± standard deviation (SD). The statistical significance was evaluated by Student's *t*-test and one-way ANOVA. P value < 0.05 was considered statistically significant.

3. Results and discussion

3.1. Synthesis and characterizations

The synthetic routes of NI-ATRA, NI-DOX and PEG-*p*Lys-NI are shown in Supporting Information Fig. S1 and all ^{1}H NMR and mass spectral are depicted in the Supporting Information Figs. S2−S10. The CMC value of PEG-*p*Lys-NI was measured to be 5.33 μg/mL (Supporting Information Fig. S11A) and the weight average Mw of copolymers was up to 7485 Da (Fig. S11B). Approximate eighteen NI are covalently linked to single polymer.

3.2. Preparation and characterizations of NM-N-NI

The PEG-*p*Lys-NI copolymers could spontaneously self-assemble into nanocore in the aqueous solutions and are used for co-encapsulating the hypoxia-activated therapeutic prodrugs, NI-DOX and NI-ATRA. During the preparation procedure, imidazole rings of copolymers and the loaded prodrugs would tend to form relatively strong intramolecular $\pi-\pi$ stacking interactions *via* the similarity-intermiscibility theory. In this way, the hydrophobic moiety linking with imidazole rings and the prodrugs would self-assemble into the core, while the PEG segment would surround outside to interact with the water molecules to decrease the potential energy. The formed N-NI showed a solid spherical form under the TEM (Fig. 1E). The particle sizes of N-NI were 78.40 ± 1.83 nm and had uniform particle size distribution tested by DLS, and its surface presented negatively charged due to a substantial number of amino groups were covalently linked to NI (Fig. 1B and C). Neutrophils were isolated from bone marrow by Percoll density gradient centrifugation and then stimulated with recombinant tumor necrosis factor-α (TNF-α)[35]. Supporting Information Fig. S15 showed that the expression of CXCR4 and CD11b is elevated with TNF-α, which suggested that neutrophils were activated successfully. The plasma membrane of the stimulated neutrophils was extracted and translocated onto the surface of N-NI as well. When the nanocore was wrapped with the neutrophil membrane (NM), a cell membrane layer with the core−shell structure was observed by TEM. The ratio of cell membranes was optimized by monitoring the changes of particle size and zeta potential values (Supporting Information Figs. S12C and D). Owing to the membrane cloaking, the zeta potential of diameter NM-N-NI was closer to the zeta potential value of NMV compared with N-NI, and the average size of NM-N-NI elevated about 14 nm in as detected by DLS, which confirmed the successful formation neutrophil-coating platforms. N-NI and NM-N-NI exhibited an average particle size distribution (Fig. S12A). Furthermore, the particle sizes and zeta potential changes in PBS for three days demonstrated the stability of NM-N-NI under physiological conditions (Supporting Information Fig. S13). Afterwards, the classic Coomassie blue assay showed that the protein

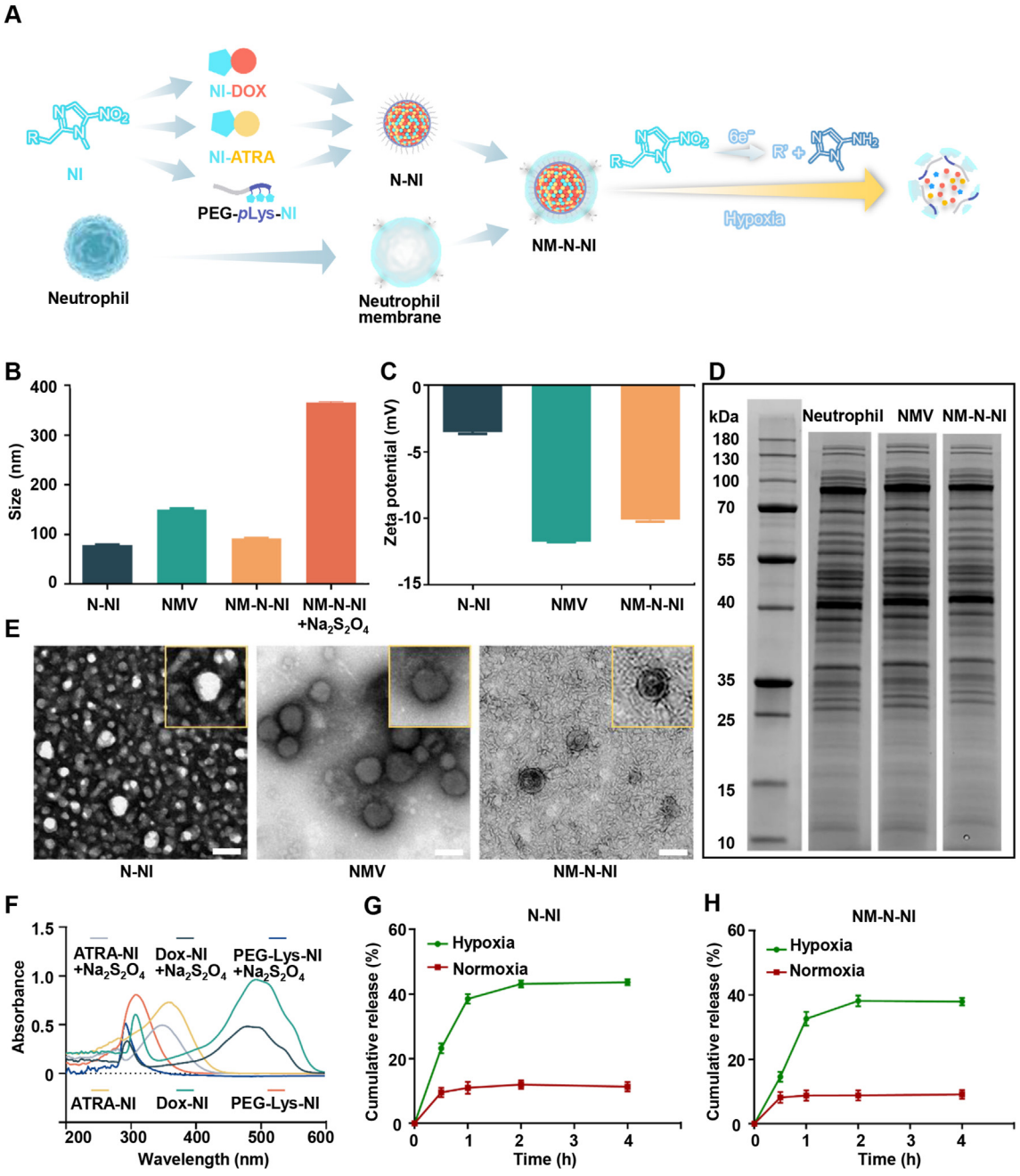

Figure 1 Preparation and characterization of NM-N-NI. (A) Schematic illustration of NM-N-NI preparation; (B) Average diameter of N-NI, NMV and NM-N-NI before and after $Na_2S_2O_4$ treatment; (C) Zeta potentials of N-NI, NMV and NM-N-NI; (D) SDS-PAGE protein tracking of the NM, NM-N-NI and neutrophils, respectively. (E) The TEM images of N-NI, NM-N-NI and NMV; (F) The UV absorption spectra of NI-DOX, NI-ATRA and PEG-*p*Lys-NI; Release from N-NI (G) and NM-N-NI (H) under normoxia mimicked hypoxia conditions. Data are presented as mean ± SD (n = 3).

profile of tracked on NM-N-NI was analogous to that of the isolated neutrophils membrane and the whole neutrophils sample, which suggested that most of the membrane protein of the neutrophils could be translocated to the surface of NM-N-NI system *via* our method (Fig. 1D).

In the hypoxic solid tumors, NI was found reduced to hydrophilic aminoimidazole (AI). This important natural has been applied in several prodrug-design (metronidazole, tirapazamine, ornidazole) that has been approved by US Food and Drug Administration (FDA) and used in clinic, with the aim of activation upon being in hypoxia microenvironment *in vivo*[36,37]. $Na_2S_2O_4$ was reported able to mimic the hypoxia condition *in vitro*, which could quickly reduce the oxygen concentration to zero and served as an electron donor for the reduction of the NI derivative[38,39]. After incubation with $Na_2S_2O_4$ (20 mmol/L) for 10 min, NM-N-NI was found gradually swelled and the particle size increased from 91.95 ± 1.56 to 366.30 ± 2.55 nm (Fig. 1B). Moreover, the retention time of PEG-*p*Lys-NI after reduction delayed by 0.8 min determined by gel permeation chromatography (GPC), likely attributable to the fact that NI was reduced and

detached from PEG-*p*Lys-NI (Fig. S12B). Moreover, the broken membrane structure was found in TEM image after incubation with Na_2S_2O (Supporting Information Fig. S14). The ultra violet (UV) was used to further test the hypoxia−responsive properties of NI-DOX, NI-ATRA and PEG-*p*Lys-NI. As shown in Fig. 1F, the UV maximum absorption peaks of NI-DOX, NI-ATRA and NM-N-NI apparently decreased and exhibited a blue shift upon being incubated with $Na_2S_2O_4$ under the mimic hypoxic condition. This was possibly due to the successful reduction of NI to aminimidazole (AI). Furthermore, since the fluorescence of NI-DOX could be quenched by $Na_2S_2O_4$, so a more stable fluorophore pyrene was chosen as an analogue to investigate the drug release kinetics under different conditions (Fig. 1G and H). Approximately 40% of pyrene in N-NI group was rapidly released within 1 h under the mimicked hypoxic condition (100 μmol/L NADPH, 2 mg/mL liver microsomes). In comparison with normoxic conditions, the release of pyrene was significantly enhanced. The release behavior of NM-N-NI exhibited the similar results with N-NI. These results suggested that under hypoxic conditions, the hydrophobic nitroimidazole moieties would convert into hydrophilic aminoimidazole, meanwhile, the imbalanced amphipathy leads to the destruction of the aggregation to release the encapsulated drugs. The generated aminoimidazole, as a typical proton sponge, would recruit more proton exteriorly to increase the osmotic pressure. Subsequently, water molecules would enter the neutrophils membrane-wrapping nanocore to destabilize the structure.

The concentration of NI-DOX and NI-ATRA was analyzed by the fluorescence spectrophotometers and HPLC, respectively (Supporting Information Fig. S16). The encapsulation efficiency (EE) of NI-DOX and NI-ATRA were 83.37% and 46.65% (Supporting Information Table S1), respectively and the drug loading rate (DL) of NI-DOX and NI-ATRA were 3.37% and 1.65%, respectively. Compared to DOX and ATRA, EE of both NI-modified prodrug was enhanced by 21.65% and 80.60%, respectively. This is attributed to the strong intramolecular $\pi-\pi$ stacking interactions between the aromatic rings after modification of nitroimidazole groups.

3.3. Cellular uptake and the internalization mechanism

The internalizing capability of the platforms into tumour cells has a direct impact on its antitumor efficiency. Hence, coumarin-6 probe was replaced with drugs for better monitoring the cellular uptake behaviors of N-NI and NM-N-NI. Supporting Information Fig. S17A−S17B shown that Coumarin-6@NM-N-NI was taken up into tumor cells in a time- and concentration-dependent manner. Moreover, fluorescence microscope image and flow cytometry showed that the intracellular fluorescence intensity of 4T1 cells incubated with Coumarin-6@NM-N-NI is relatively higher than that of Coumarin-6@N-NI group (Supporting Information Figs. S17C and S18). To further explore the endocytosis mechanism of Coumarin-6@NM-N-NI, the cellular uptake efficiency was performed in the presence of varieties of inhibitors (filipin, chlorpromazine and wortmannin). Flow cytometry analysis illustrated that the cellular internalization of Coumarin-6@N-NI in 4T1 cells was effectively inhibited by filipin, which suggested that Coumarin-6@N-NI could be ingested by 4T1 cells *via* a caveolin-mediated and energy-dependent endocytic pathway (Fig. 2B). In contrast, in the Coumarin-6@NM-N-NI group, filipin and wortmannin inhibit the cellular uptake effectively (Fig. 2C), indicating a caveolae and macro-pinocytosis-mediated endocytosis pathway of Coumarin-6@NM-N-NI and the involvement of lysosome therein. This might be due to the membrane attachment inducing a differential endocytic modality for Coumarin-6@NM-N-NI. Furthermore, the platforms were labeled with coumarin-6 and intracellular behavior of Coumarin-6@NM-N-NI was also observed by confocal laser scanning microscopy (CLSM). A fraction of the green coumarin-6 and red lysotracker (lysosomal probes) displayed orange and yellow colocalization to each other in the first 0.5 h, whereas after 2 h, most of the green fluorescence dots were found isolated from the red ones. It was inferred that Coumarin-6@NM-N-NI probably entered 4T1 cells *via* the caveolae and macro-pinocytosis-mediated endocytosis pathway upon interacting with the tumor cell membrane. Then, due to the overexpression of nitroreductase and NADPH quinone dehydrogenase 1 (NQO1) in the cytoplasm, nitroimidazole groups on the side chain of polylysine were reduced to aminoimidazole and rapidly shed. Subsequently, the newly exposed amino created the extra positive charge, inducing Coumarin-6@N-NI to escape from lysosomes after neutrophil membrane fused with the lysosomal membrane. When NI-DOX and NI-ATRA were co-encapsulated by NM-N-NI, once NI-D/A@NM-N-NI finished the escape behavior, it would synchronously release the loaded prodrugs, which could be further reduced to release DOX and ATRA respectively under the same hypoxic condition. As shown in Fig. 2F, the tumor cells cultured with NI-D/A@NM-N-NI exhibited a notably augment in apoptosis rate (the early and late apoptosis rate was about 24.45% and 46.69%, respectively), which could be attributed to the elevated internalization efficiency and fast intracellular drug release.

The cell counting kit-8 (CCK-8) assay was employed to further assess the cytotoxicity of NI-D/A@NM-N-NI on 4T1 cells. As shown in Supporting Information Fig. S19, and Tables S2 and S3, the obtained IC_{50} values of the NI-D/A@NM-N-NI group at hypoxic conditions were 1.22 μmol/L NI-DOX and 0.49 μmol/L NI-ATRA, respectively, which were lower than other groups. Moreover, CI values lower than 1 in NI-D/A@NM-N-NI indicated synergistic effect of the combination of that DOX and ATRA. Similar trends were also found in normoxic conditions.

3.4. Redox imbalance and inhibition of stemness-related properties

Tumor cells redox adaptation is emerging as a crucial factor in tumorigenesis, cancer invasion, metabolism, and drug resistance. By the way, this is also one of the important triggers in designing stimuli-responsive drug delivery system, most of which, however, could favorably accomplish the passive command−driven activity instructed by one the redox couples, while few systems could reversely and simultaneously adjust the intracellular redox balance. This is due to the dynamic redox microenvironment maintained by the continuous formation of the redox species from mitochondria, cytoplasm and other organelles, which requires the tailoring species with high oxidation or reduction state (for instance, from nitro (+3 valence) to amine (−3 valence)). The $NADP^+$/NADPH redox couples are crucial in the maintenance of intracellular redox homeostasis and modulation of multiple biological processes. During the bio-reduction process of single NI, three NADPH is consumed with six electrons being transferred, and single polymer would exhaust 54 NADPH, which drastically impacted the redox balance. Hence, oxidative stress induced by nitroimidazole can be amplified by down-regulating GSH and up-regulating ROS at the same time, which could be an effective

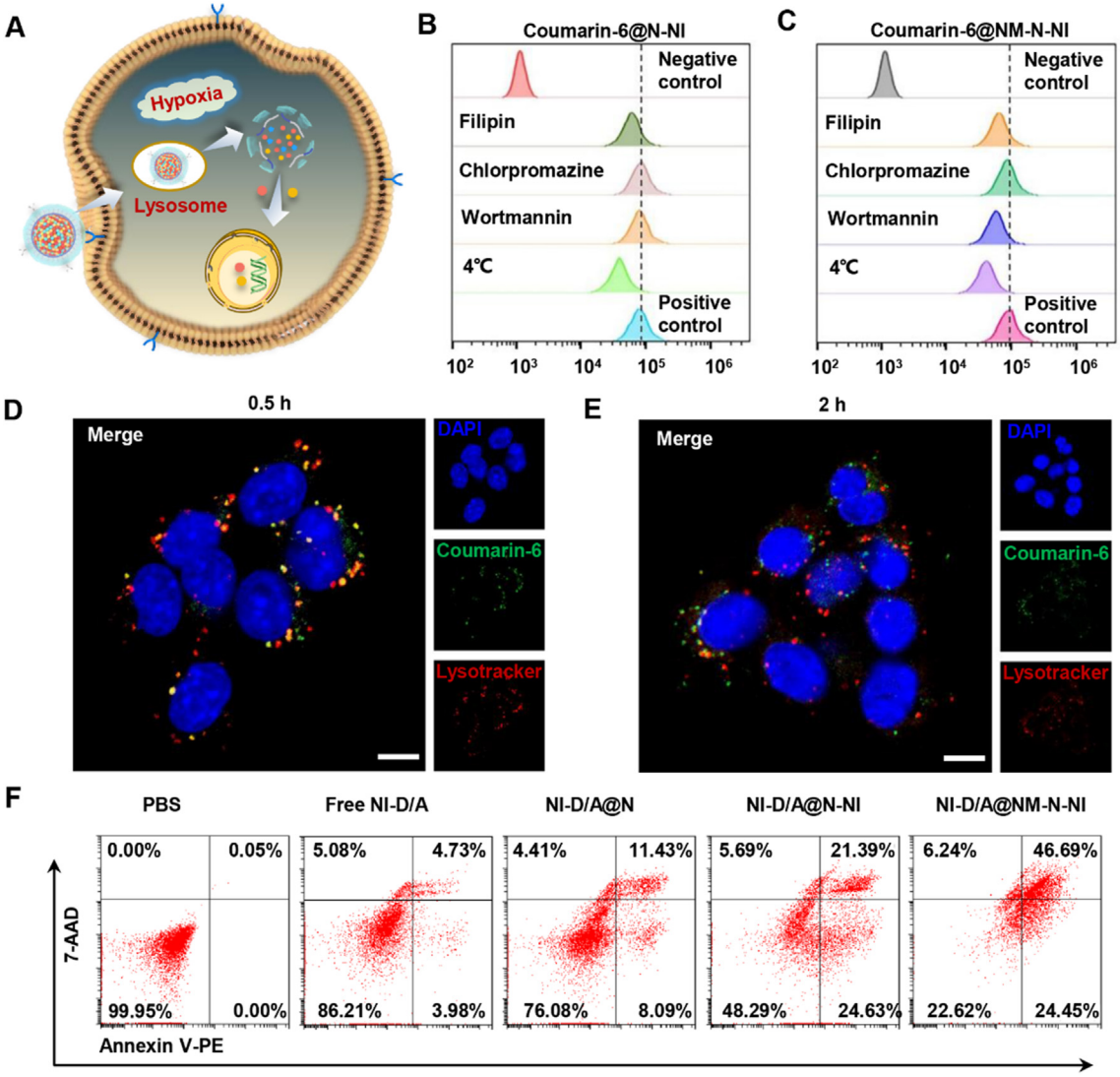

Figure 2 Cellular uptake and the internalization mechanism of neutrophil-like hypoxia-responsive platforms. (A) Illustration of cellular uptake of NM-N-NI; flow cytometry analysis of (B) N-NI and (C) NM-N-NI endocytosis pathway blocked by different inhibitors; CLSM image of the intracellular behavior of NM-N-NI in (D) 0.5 h and (E) 2 h. Scale bar = 20 μm. (F) Tumor cells apoptosis incubated with PBS, free NI-DOX and NI-ATRA (Free NI-D/A), NI-DOX and NI-ATRA co-encapsulated nanoparticles assembled with PEG-*p*Lys-NCA (NI-D/A@N), N-NI nanocore co-encapsulated with NI-DOX and NI-ATRA (NI-D/A@N-NI), and NI-D/A@N-NI coated with NM (NI-D/A@NM-N-NI).

strategy to prevent tumor cells retro-differentiation into BCSCs and enhance tumor sensitivity to chemotherapy.

The $NADP^+$/NADPH ratio can be used as the indicator to evaluate the potency of electron-accepting nanosystem in consuming NADPH under hypoxia conditions. As illustrated in Fig. 3B, under normoxia, both NI-D/A@N-NI and NI-D/A@NM-N-NI would not cause the obvious alteration of $NADP^+$/NADPH ratio compared to free NI-D/A in the 4T1 cells. Nevertheless, such a ratio remarkably elevated for NI-D/A@NM-N-NI under hypoxia due to NADPH depletion (Fig. 3C). NI-D/A@NM-N-NI was superior over NI-D/A@N-NI with regard to transient NADPH consumption in hypoxic cells. Similarly, NI-D/A@NM-N-NI did not diminish the intracellular GSH level of under normoxia (Fig. 3D). However, under hypoxia conditions, a tendency to decrease was were observed for GSH upon NI-D/A@NM-N-NI supplementing to 4T1 cells and the decline extent was greater as compared to NI-D/A@N-NI group (Fig. 3E). This suggested that the tumor cell uptake was enhanced after N-NI was coated with neutrophil membrane and more nitro groups were rapidly reduced to amino groups to regulate the interplay between GSH/GSSG and NADPH/$NADP^+$ in the intracellular levels.

The cell-permeable singlet oxygen sensor DCFH-DA was used to further evaluated the mechanism of action, which can be oxidized by singlet oxygen to generate fluorescent DCF. 4T1 cells incubated with PBS or free NI-D/A displayed weak green fluorescence under normoxia and hypoxia conditions, suggesting that the intracellular level of ROS is lowering (Fig. 3F and G). Nevertheless, 4T1 cells incubated with NI-D/A@N-NI exhibited relatively stronger fluorescence signals under hypoxia in result of the reduction of GSH. NI-D/A@NM-N-NI was more potent than the NI-D/A@N-NI in reducing GSH and enhancing ROS level, which could be attributed to the elevated internalization efficiency of the neutrophil-like platforms. Therefore, NI-D/A@NM-N-NI was regarded capable to significantly amplify the oxidative

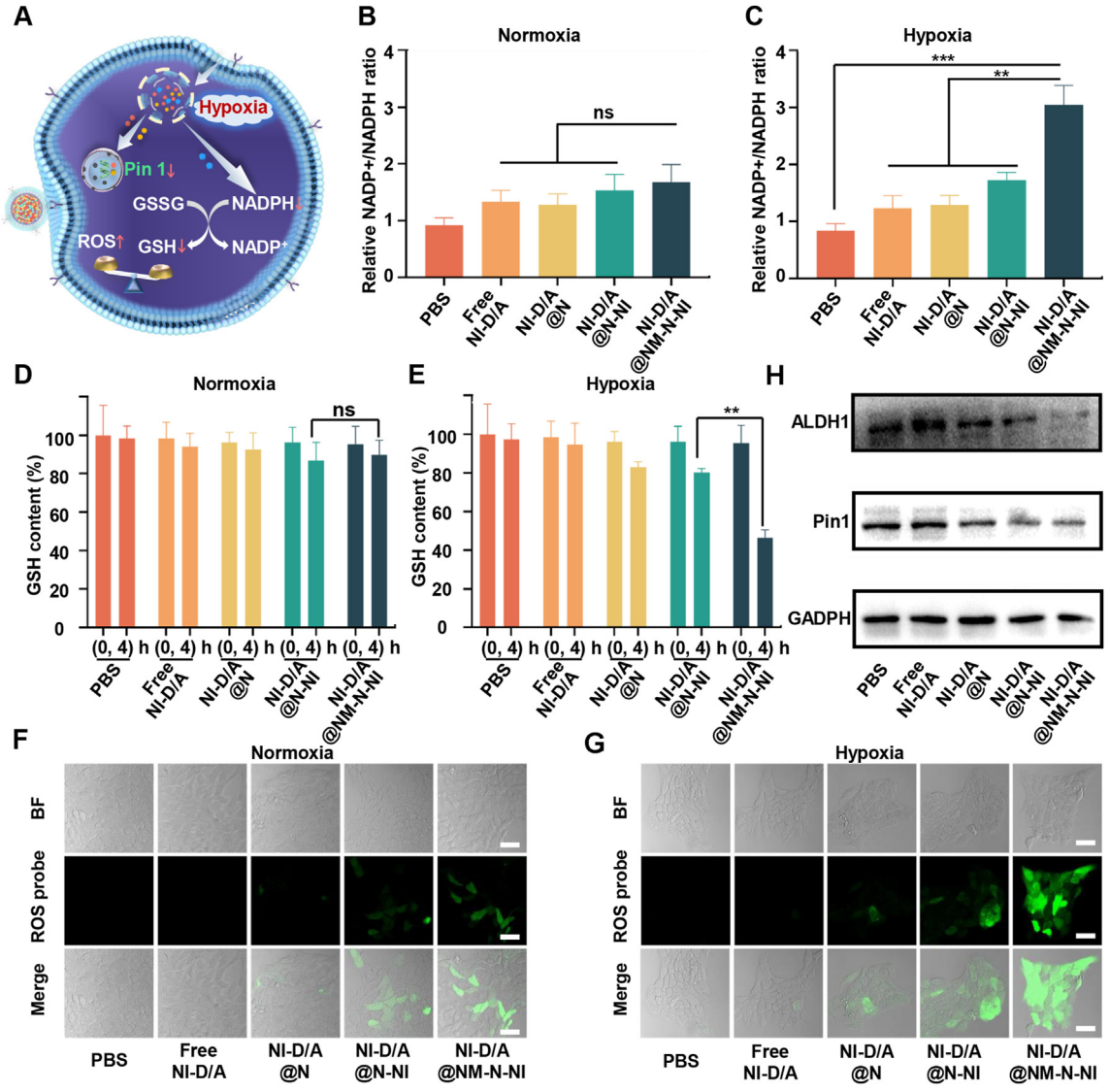

Figure 3 Redox imbalance and inhibition of stemness-related properties of neutrophil-like hypoxia-responsive platforms. (A) Cellular mechanism illustration of NM-N-NI; Relative intracellular $NADP^+$/NADPH ratio in 4T1 cells under normoxic (B) or hypoxic (C) conditions. Data are presented as mean ± SD ($n = 3$). $^{**}P < 0.01$, $^{***}P < 0.001$. ns, not significant; Glutathione (GSH) level in 4T1 cells under normoxic (D) or hypoxic (E) conditions, Data are presented as mean ± SD ($n = 3$). $^{**}P < 0.01$. ns, not significant; Fluorescent imaging of reactive oxygen species (ROS) in 4T1 cells under normoxic (F) or hypoxic (G) conditions. Scale bar = 50 μm; (H) Expression of ALDH1 and Pin1 in 4T1 cells determined by Western blot assay.

stress by depleting NADPH, down-regulating GSH and up-regulating ROS at the same time under hypoxia conditions. It has been reported that the extremely high level of intracellular GSH in the hypoxic tumor cell can sweep some ROS and induce chemoresistance. Hence, the disruption of redox balance induced by nitroimidazole was an effective strategy to enhance chemotherapeutic sensitivity of tumor cells.

Then, the combination effects of the differentiation therapy and hypoxia-activated chemotherapy on eliminating BCSCs *in vitro* was evaluated. Breast cancer cells with $ALDH1^+$ phenotypes have been demonstrated to have stem cell-like tumor-initiating and invasive features[40,41]. Firstly, we enriched 4T1 BCSCs with $ALDH1^+$ phenotypes by ALDEFLUOR™ Kit and the proportion of BCSCs was 15.07%, and then culture them to form mammosphere in the serum-free medium (Supporting Information Figs. S21A and B). The formed tumor spheres contribute to maintaining the stemness of BCSCs in specific micro-environment (such as hypoxia and starvation), which models the status of solid tumor tissues *in vivo*. The population of $ALDH^+$ cells was measured using ALDEFLUOR after mammospheres were treated with PBS, free NI-D/A, NI-D/A@N, NI-D/A@N-NI, NI-D/A@NM-N-NI. Fig. S21D showed that the proportion of BCSCs in free NI-D/A group (13.69%) was moderately lower than that in the PBS group (17.49%). The ALDH + cells level was reduced after NI-D/A@N-NI treatment, which decreased by 48.3% compared with NI-D/A@N treatment. This is because hypoxia-activated carrier

materials result in a burst drug release. The NI-D/A@NM-N-NI treatment of 4T1 cells remarkably reduced the percentage of $ALDH^+$ cells as compared with NI-D/A@N group, which was only 1.78%.

Prolyl-isomerase Pin 1 plays a prominent role in induction and maintenance of BCSCs self-renewal and ALDH1 activity is a common marker of the stemness of breast cancer cells[20,42,43]. Therefore, in order to further investigate the mechanism of eliminating BCSCs, the expression level changes of Pin1 and ALDH1 proteins were evaluated by immunohistochemistry assay and Western blot analysis. The Western blot analysis demonstrated that the higher expression of Pin1 and ALDH1 was observed in PBS group and free NI-D/A group, while their significantly down-regulated expression was observed in NI-D/A@NM-N-NI group (Fig. 3H and Supporting Information Fig. S20). In Fig. S21C, the colocalization of Pin1 with ALDH1 protein was found in mammospheres. The higher expression of green Pin1 and red ALDH1 was observed in PBS group and free NI-D/A group, and almost no signal was observed in NI-D/A@NM-N-NI group, which indicated that NI-D/A@NM-N-NI could inhibit the expression of Pin1 and further eliminate BCSCs.

Based on the above results, when the neutrophil-biomimic hypoxia-activated platform reach the hypoxia region, both prodrugs of ATRA and DOX were released rapidly. ATRA-induced Pin1 ablation can promote the differentiation of BCSCs into non-BCSCs, reducing their self-renewal capacity and simultaneously substantial reduction of nitroimidazole consumed the NADPH and disrupted the redox equilibrium in tumor cell. The oxidative stress was amplified by down-regulating GSH and up-regulating ROS, which prevent retro-differentiation process from non-BCSCs to BCSCs and enhanced the sensitivity of tumor cells towards DOX. These results suggested that the BCSCs differentiation and tumor microenvironment modulation synergistically could enhanced chemotherapeutic cytotoxicity and concurrently eliminate the non-BCSCs and BCSCs.

3.5. *In vivo metastasis targeting and biodistribution in the breast cancer model*

In order to assess the lung metastasis-targeting characteristics of the designed platforms, we constructed 4T1-luciferase lung metastasis mice models and used Did NIR probe as an analogue for better monitoring the drug distribution by visual techniques. As shown in Fig. 4D, Did fluorescent signals were detected using IVIS imaging system in the metastatic lung administered with free Did and Did-labeled platforms 1-24 h post injection. The weak Did signal was observed in the lung in free Did group and Did@NM-N-NI group exhibited much stronger fluorescent intensity in the lung than free Did, Did@N and Did@N-NI group. At 24 h after intravenous administration, the fluorescence images of *ex vivo* organ showed that the fluorescence signal chiefly distributed in the liver and lung in Did@NM-N-NI group and distributed in the liver in other groups (Fig. 4A). The quantification analysis of neutrophil-like hypoxia-responsive platforms was further evaluated by comparing the biodistribution of Did in the lung metastatic models. As shown in Supporting Information Fig. S22, Did in the lung displayed a high drug accumulation of 89.43 (μg/g) 4 h after injection of Did@NM-N-NI, which was 2.1- and 1.7-fold higher than those of free Did and Did@N-NI groups, respectively. At 24 h post administration, Did@NM-N-NI group elevated the Did concentration to be 3.6- and 2.4-fold than free Did and Did@N-NI groups, respectively (Fig. 4B). In order to further verify drug accumulation at lung metastatic lesion, coumarin-6 labeled platforms was visualized in 4T1-ERFP metastatic lung section by CLSM (Fig. 4C). Almost no green coumarin-6 fluorescence was observed at the red ERFP-labeled metastatic sites in the free coumarin-6 group and coumarin-6 fluorescence intensity were enhanced in coumarin-6@N-NI group due to size effect at tumor sites. In the coumarin-6@NM-N-NI group, the increased green fluorescence was observed in the peripheral region, outer side, and inner side of the red metastatic nodules, indicating that upon being coated with neutrophils membrane to N-NI, the neutrophil-like platforms inherited the neutrophil capacity of actively targeting metastatic cancer cells and accumulated in the lung metastasis sites.

In order to assess the primary tumor-targeting characteristics of the designed platforms, we constructed 4T1-luciferase primary mice models. As shown in Supporting Information Fig. S23, a small amount of Did fluorescence was observed in the tumor in free Did group and Did@NM-N-NI group exhibited much stronger fluorescent intensity in the tumor than free Did and Did@N-NI group. At 24 h after intravenous administration, the fluorescence images of *ex vivo* tumor showed that an intense fluorescence signal of tumor was exhibited in Did@NM-N-NI group (Supporting Information Fig. S24).

3.6. *In vivo anti-metastatic efficacy in lung metastasis model*

To evaluate whether the platforms can control the outgrowth of already formed lung metastases of TNBC, luciferase signals from the 4T1-luci cells were monitored using IVIS Spectrum to represent the regions of lung metastasis after treatments. As illustrated in Fig. 7B and C, the higher metastatic lung signals were exhibited in the saline, free D/A, free NI-D/A and blank N-NI group, while NI-D/A@N-NI displayed less luciferase signals. Further, in neutrophil-like NI-D/A@NM-N-NI group, extremely faint signal was observed in comparison with the NI-D/A@N-NI group. The lung metastatic nodules analysis was similar to these results. The lungs of the mice were rinsed with saline, and blank N-NI and free drug group were thickly dotted with metastatic nodules and the 4T1 tumor burdens of H&E-stained lung section images covered most area (Fig. 5F). The NI-D/A@N-NI and NI-D/A@NM-N-NI groups exhibited less metastasis foci, with average metastatic nodule numbers decreased by 45.4% and 74.2% compared with the saline group, respectively, which increased the inhibition rate on lung metastasis to 63.2% and 83.2%, respectively (Fig. 5D−E and Supporting Information Fig. S25B). Lung metastasis mice showed the longest survival time upon receiving the NI-D/A@NM-N-NI treatment, compared with the mice in other groups (Fig. S25C).

During the treatment, multi-round chemotherapy results in the augment of the BCSCs fraction in the tumor, and these drug-resistant cells are more likely to survive and potential to spread to distant sites. The disseminated BCSCs will immediately proliferate and colonize into new environment, but some BCSCs will enter a dormant state and form dormant microcluster. They would maintain tumor cell stemness, remain resistant to cytotoxic drugs, and eventually form lethal macrometastasis. Therefore, we further explored the capability and mechanism of neutrophil-like hypoxia-responsive platforms to eradicate BCSCs in lung metastasis site. As illustrated in Supporting Information Fig. S26, the higher expression of green Pin1 and red stemness markers (ALDH1) was observed in saline group and exhibited co-localization. Weaker

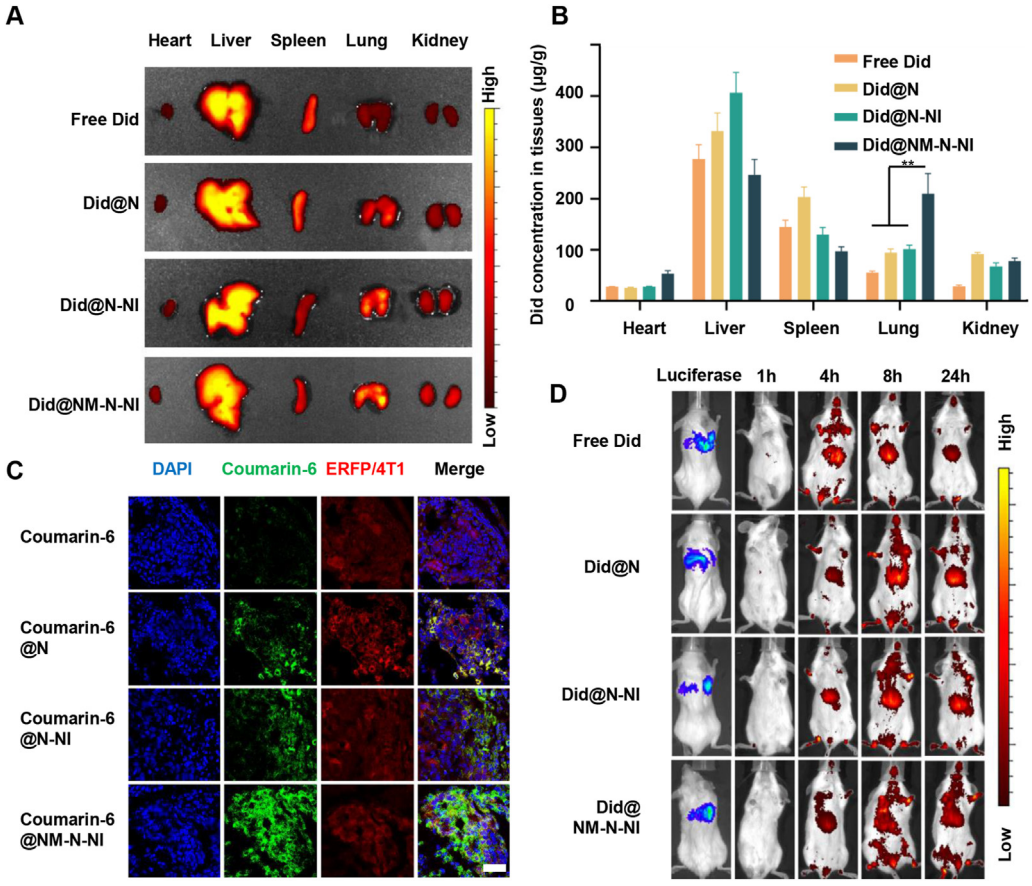

Figure 4 *In vivo* metastasis targeting and biodistribution of different formulations in lung metastasis model. (A) *In vivo* Did biofluorescence images of different organs following injection of free Did, Did-labeled nanoparticles assembled with PEG-pLys-NCA (Did@N), Did-labeled N-NI (Did@N-NI) and Did-labeled NM-N-NI (Did @NM-N-NI); (B) Quantified distribution of different Did-labeled formulations in major organs at 24 h post-injection. Data are presented as mean ± SD ($n = 3$), $^{**}P < 0.01$; (C) CLSM images of different formulations in metastatic lung tissues following injection of free coumarin-6, coumarin 6-labeled nanoparticles assembled with PEG-*pLys*-NCA (coumarin 6@N), coumarin 6-labeled N-NI (coumarin 6@N-NI) and coumarin 6-labeled NM-N-NI (coumarin 6@NM-N-NI). Scale bar = 100 μm. (D) *In vivo* fluorescence images of lung metastasis mice at different times after intravenous injections of free Did, Did@N, Did@N-NI, Did@NM-N-NI.

expression of Pin1 and ALDH1 was observed in NI-D/A@N-NI group as compared to NI-D@N-NI and NI-A@N-NI group and almost none was found in NI-D/A@NM-N-NI group, which indicated that NI-D/A@NM-N-NI could inhibit the expression of Pin1 and further suppress aggressive phenotypes through BCSCs exhaustion. Pin1 is a *bona fide* stem cell factor and high Pin1 levels are crucial in maintaining the self-renewal and replicative potential of BCSCs of the mammary gland. It suggested that NI-D/A@NM-N-NI could actively accumulated in the lung metastasis lesion relying on the targeting capacity of neutrophils, rapidly reduced and released ATRA and DOX under hypoxic condition. Subsequently, high concentration of ATRA induced the ablation of Pin1 to promote BCSCs differentiation and simultaneously prevent non-BCSCs retro-differentiation to elicit sensitivity to DOX. TUNEL assay was further used to evaluate the apoptotic 4T1 cells in the metastatic foci (Fig. 5F). The intense red apoptosis signals were observed in NI-D/A@N-NI group, which induced more tumor cell death as compared to either NI-D@N-NI or NI-A@N-NI group. The highest apoptosis signal was found in NI-D/A@NM-N-NI group, which suggested better inhibition effect of metastasis by combining differentiation therapy and tumor microenvironment modulation.

3.7. *In vivo antitumor efficacy in primary tumor model*

To further verify whether the neutrophil-like hypoxia-responsive platforms (NI-D/A@NM-N-NI) could effectively inhibit primary tumor growth on the BCSCs-enriched tumor model, we treated 4T1 orthotropic tumor mice with NI-D/A@NM-N-NI or various formulations through intravenous injection every two days from Day 14 of postimplantation of tumor cells. As shown in Fig. 6B, C and E, free D/A and free NI-D/A could slightly inhibit the tumor growth, while the NI-D/A@N treatment could just slightly increase the inhibition at the same doses. Encouragingly, NI-D/A@NM-N-NI group exhibited the highest inhibition capacity on tumor growth compared with other formulation. Moreover, the H&E staining images and TUNEL assay showed that treatment with NI-D/A@NM-N-NI led to extensive cell necrosis in most tumor area (Fig. 6G). Subsequently, to further investigate the therapeutic potential mechanisms of the combined differentiation therapy and hypoxia-activated chemotherapy on cancer stem cells *in vivo*, relative $NADP^+$/NADPH ratio and the proportion of BCSCs ($ALDH^+$) recovered from the tumors was examined at the end of the treatments. The NI-D/A@NM-N-NI treatment enhanced $NADP^+$/NADPH ratio (Supporting Information Fig. S27) and evidently reduced the proportion of $ALDH^+$ cells in

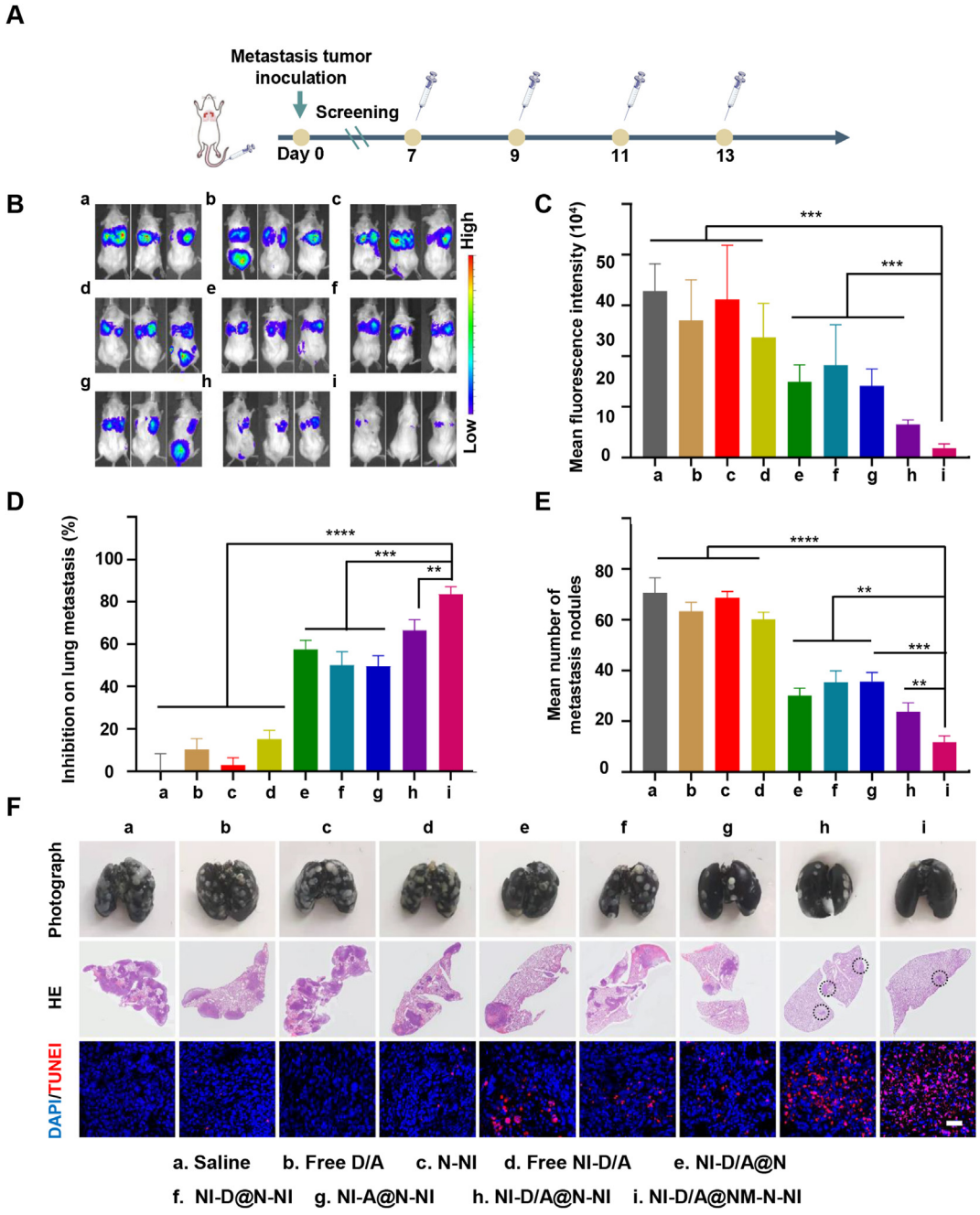

Figure 5 Therapeutic effects on lung metastases of breast cancer. (A) Timeline for lung metastasis models establishment and treatment schedule; (B) Real-time bioluminescence images; (C) semi-quantitative results of bioluminescence signals of lung metastases; (D) The inhibition rate on lung metastasis of various groups compared to the saline control; (E) The average number of lung metastatic nodules from each group. (F) Typical images of lung tissues, HE staining images of metastatic foci in lungs from each group and TUNEL assay (Scale bar: 100 μm). The metastatic nodules were denoted as white spots in lungs. Data are presented as mean ± SD ($n = 3$). $^{**}P < 0.01$, $^{***}P < 0.001$, $^{****}P < 0.0001$.

solid tumors (Fig. 6D and Supporting Information Fig. S29A). We further probed the potential mechanisms of anti-tumor *in vivo* by the immunofluorescence and Western blot. The higher expression of Pin 1, ALDH1 and CD44 was observed in saline group. However, the NI-D/A@NM-N-NI could significantly decrease the expression of Pin1 and further reduce the expression of stemness marker ALDH1 and CD44 (Fig. 6F, Figs. S29B and S30). In addition to the cytotoxic therapy on primary tumors, loss of the BCSCs populations would retard the formation of micro-metastasis. As illustrated in H&E images of lung (Fig. 6G), the blue-colored micrometastasis of lung was not found in NI-D/A@NM-N-NI group, but appeared in other groups. These data confirmed that NI-D/A@NM-N-NI could carry high concentration of nitroimidazole group to consume the NADPH under hypoxic tumor region, further disrupt the redox equilibrium and amplify oxidative stress to enhance the sensitivity of tumor cell towards

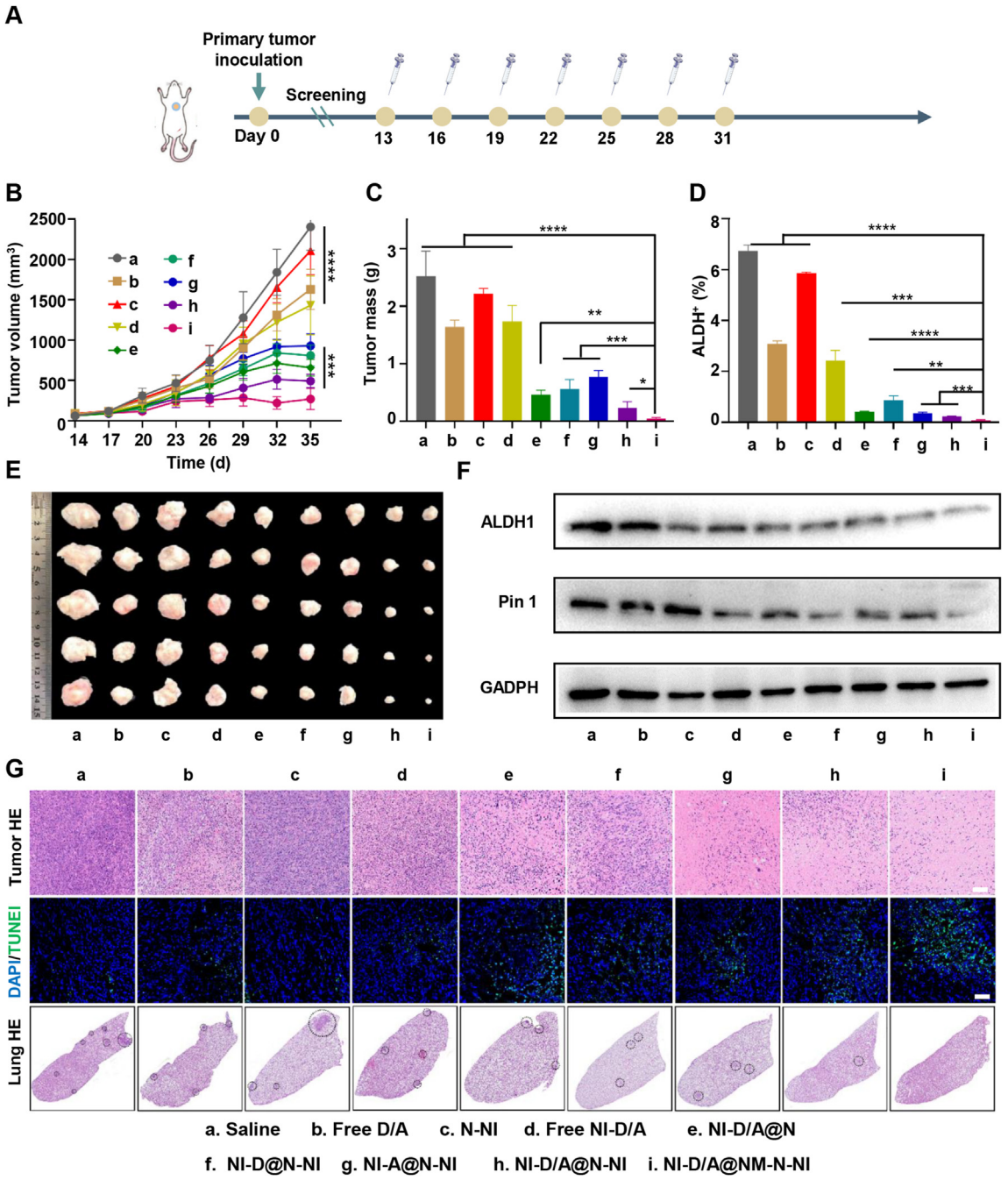

Figure 6 Therapeutic effects on breast primary tumor. (A) Timeline for primary tumor models establishment and treatment schedule; (B) Tumor growth curves of various groups. (C) Tumor mass of various groups. (D) The $ALDH^+$ cells proportion within solid tumors after the tumor suppression study. (E) The tumor images of various groups. (F) Expression of ALDH1 and Pin 1 in tumor determined by Western blot assay; (G) Representative HE staining images of tumor and lung, and TUNEL assay of tumor (Green: TUNEL for staining apoptotic cells and blue: DAPI for staining cell nucleus, Scale bar = 100 μm). Data are presented as mean ± SD ($n = 5$). *$P < 0.05$, **$P < 0.01$, ***$P < 0.001$, ****$P < 0.0001$.

DOX. Moreover, the released ATRA induced Pin1 ablation in BCSCs, promote the differentiation of BCSCs into non-BCSCs, and increasing their sensitivity to chemotherapeutic drugs. Inhibition of Pin1 in non-BCSCs prevents the retro-differentiation process from non-BCSCs to BCSCs. In a word, the new combinations of differentiation therapy and tumor microenvironment modulation synergistically amplify tumor cellular sensitivity to DOX, concurrently eliminate the non-BCSCs and BCSCs and eventually satisfies the demand for promoting a maximized synergistic anti-tumor efficacy.

3.8. *In vivo safety evaluation*

To evaluate the initial biosafety of the NM-N-NI platforms, main organs including heart, liver, spleen, lung, and kidney were stained with H&E. No apparent histological damage or inflammation were found in platform-treated groups (Fig. 7E), indicating favorable compatibility of the platforms. Moreover, biochemical analysis was also performed on the blood samples to further investigate the potential side effects of the platforms. The parameters related with liver function markers (AST, aspartate transaminase; ALT, alanine

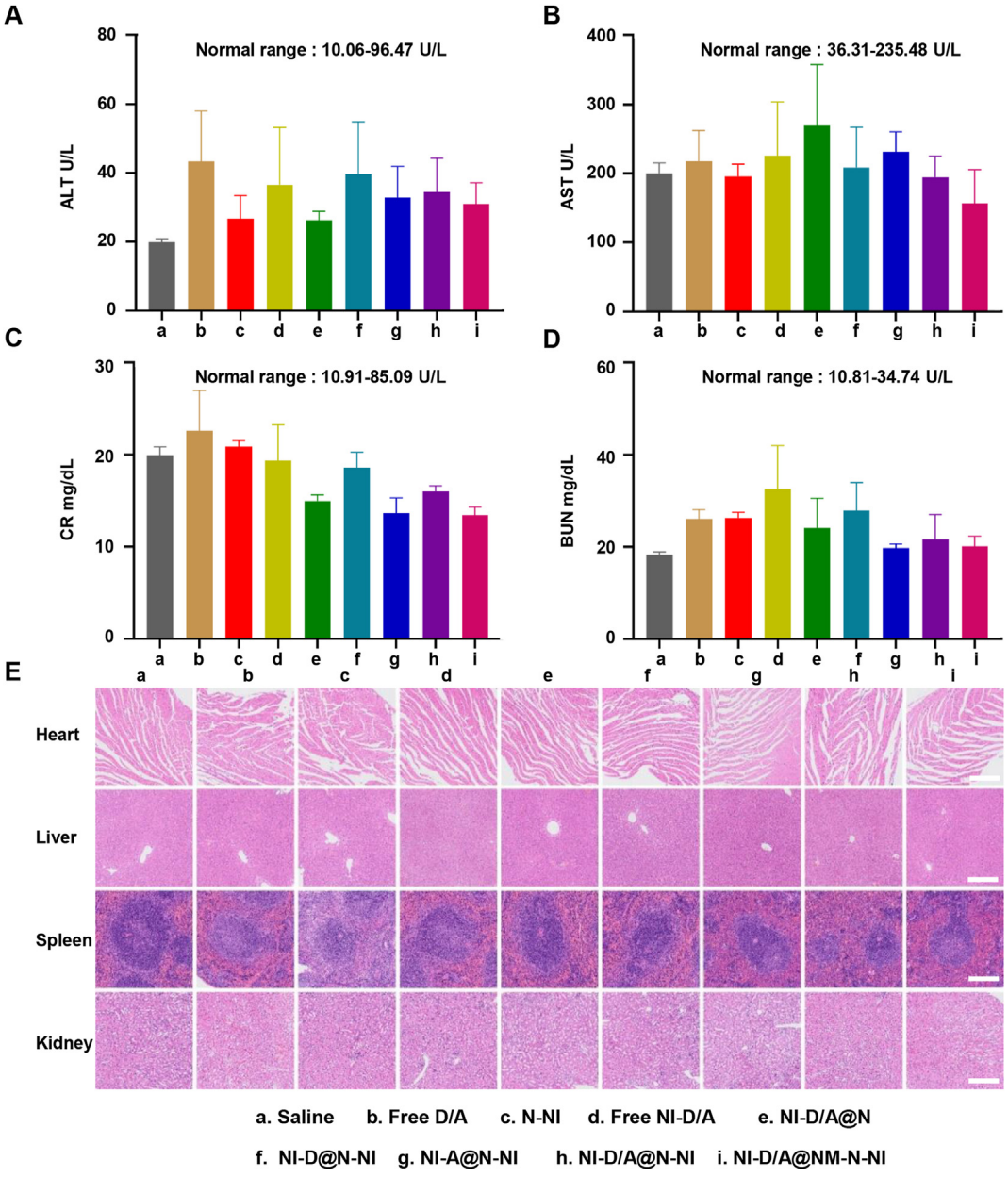

Figure 7 The biosafety assessments. (A−D) Biochemical analysis results of alanine transaminase (ALT), aspartate transaminase (AST), creatinine (CRE) and blood urea nitrogen (BUN) in the blood from different mice. Data are presented as mean ± SD (n = 3). (E) Representative hematoxylin and eosin (HE) images of main organ sections from different mice treated with different formulations. Scale bars = 200 μm.

transaminase), or kidney function markers (BUN, blood urea nitrogen; CRE, creatinine) were monitored. As illustrated in Fig. 7 A−D, the blood chemistry analysis of the NM-N-NI group was within the safe range. Moreover, the NI-D/A@NM-N-NI treatments didn't to lead to significant body weight loss (Fig. S25A and Supporting Information Fig. S28) and obvious hemolysis (Supporting Information Fig. S30), suggesting that the neutrophil-like hypoxia-responsive platforms would be potentially safe for breast cancer therapy. These results collectively demonstrated that the neutrophil-biomimic hypoxia-responsive platforms have excellent biologically safe, which is important for their safe medical applications.

4. Conclusions

Under present insufficient surgery, chemotherapy and radiotherapy for metastatic TNBC, many functionalized delivery platforms have been development to target breast cancer metastatic cells to yield effective inhibition of tumor growth. Among them, bionic platforms have been proved to be of great value[44−48]. In this study, we established a neutrophil-like targeting platform with a hypoxia-responsive drug-release characteristic to achieve high degree of enrichment of drug in lung metastasis foci of TNBC. When the multifunctional platforms reach to metastasis sites relying on the naturally targeting capability of neutrophil to

metastatic tumor cells, the modified NI groups are rapidly reduced to amino-imidazole and both differentiation agents (ATRA) and chemotherapy drug (DOX) were explosively released. During the responsiveness, ATRA could differentiate BCSCs into non-BCSCs, and simultaneously the nitroimidazole moieties on the polymer and prodrugs could modulate the tumor microenvironment by depleting NADPH and amplifying intracellular oxidative stress to prevent tumor cells retro-differentiation into BCSCs. This new combination of differentiation therapy and tumor microenvironment modulation synergistically amplify tumor cellular sensitivity to DOX, concurrently eliminate the non-BCSCs and BCSCs and eventually satisfies the demand for promoting a maximized synergistic anti-tumor efficacy.

Acknowledgments

This work was supported by National Natural Science Funds of China (92059110/81872808, China), Development Fund for Shanghai Talents (2020090, China), FDU 2025-Excellence Program Fund (China), Program of Shanghai Academic Research Leader (18XD1400500, China), Project Supported by Shanghai Municipal Science and Technology Major Project (2018SHZDZX01, China) and ZJLab.

Author contributions

Yongchao Chu, Chen Jiang, and Tao Sun designed the research. Yongchao Chu and Tao Sun carried out the experiments and performed data analysis. Yifan Luo, Boyu Su, Chao Li, Qin Guo and Yiwen Zhang assisted the synthesis of polymers and prodrugs. Peixin Liu, Hongyi Chen, Zhenhao Zhao, Zheng Zhou and Yu Wang assisted the *in vivo* therapeutic evaluations. Yongchao Chu and Tao Sun wrote the manuscript. Chen Jiang revised the manuscript. All of the authors have read and approved the final manuscript.

Conflicts of interest

The authors have no conflicts of interest to declare.

Appendix A. Supporting information

Supporting data to this article can be found online at https://doi.org/10.1016/j.apsb.2022.05.027.

References

1. DeSantis CE, Ma J, Gaudet MM, Newman LA, Miller KD, Goding SA, et al. Breast cancer statistics. *CA Cancer J Clin* 2019;**69**:438−51. 2019.
2. Bianchini G, Balko JM, Mayer IA, Sanders ME, Gianni L. Triple-negative breast cancer: challenges and opportunities of a heterogeneous disease. *Nat Rev Clin Oncol* 2016;**13**:674−90.
3. Jin L, Han B, Siegel E, Cui Y, Giuliano A, Cui X. Breast cancer lung metastasis: molecular biology and therapeutic implications. *Cancer Biol Ther* 2018;**19**:858−68.
4. Wu SY, Wang H, Shao ZM, Jiang YZ. Triple-negative breast cancer: new treatment strategies in the era of precision medicine. *Sci China Life Sci* 2021;**64**:372−88.
5. Arnedos M, Vicier C, Loi S, Lefebvre C, Michiels S, Bonnefoi H, et al. Precision medicine for metastatic breast cancer—limitations and solutions. *Nat Rev Clin Oncol* 2015;**12**:693−704.
6. Patel NR, Pattni BS, Abouzeid AH, Torchilin VP. Nanopreparations to overcome multidrug resistance in cancer. *Adv Drug Deliv Rev* 2013;**65**:1748−62.
7. Tan T, Wang YQ, Wang J, Wang ZW, Wang H, Cao HQ, et al. Targeting peptide-decorated biomimetic lipoproteins improve deep penetration and cancer cells accessibility in solid tumor. *Acta Pharm Sin B* 2020;**10**:529−45.
8. Miller MA, Gadde S, Pfirschke C, Engblom C, Sprachman MM, Kohler RH, et al. Predicting therapeutic nanomedicine efficacy using a companion magnetic resonance imaging nanoparticle. *Sci Transl Med* 2015;**7**:183−314.
9. Schroeder A, Heller DA, Winslow MM, Dahlman JE, Pratt GW, Langer R, et al. Treating metastatic cancer with nanotechnology. *Nat Rev Cancer* 2011;**12**:39−50.
10. Denny WA. The role of hypoxia-activated prodrugs in cancer therapy. *Lancet Oncol* 2000;**1**:25−9.
11. Kitamura T, Qian BZ, Pollard JW. Immune cell promotion of metastasis. *Nat Rev Immunol* 2015;**15**:73−86.
12. Powell DR, Huttenlocher A. Neutrophils in the tumor microenvironment. *Trends Immunol* 2016;**37**:41−52.
13. Szczerba BM, Castro-Giner F, Vetter M, Krol I, Gkountela S, Landin J, et al. Neutrophils escort circulating tumour cells to enable cell cycle progression. *Nature* 2019;**566**:553−7.
14. Yu PF, Huang Y, Han YY, Lin LY, Sun WH, Rabson AB, et al. TNFalpha-activated mesenchymal stromal cells promote breast cancer metastasis by recruiting CXCR2(+) neutrophils. *Oncogene* 2017;**36**:482−90.
15. Qiao Q, Liu X, Yang T, Cui KX, Kong L, Yang CL, et al. Nanomedicine for acute respiratory distress syndrome: the latest application, targeting strategy, and rational design. *Acta Pharm* 2021;**11**:3060−91.
16. Chu D, Dong X, Zhao Q, Gu J, Wang Z. Photosensitization priming of tumor microenvironments improves delivery of nanotherapeutics *via* neutrophil infiltration. *Adv Mater* 2017;**29**:1701021.
17. Shibue T, Weinberg RA. EMT, CSCs, and drug resistance: the mechanistic link and clinical implications. *Nat Rev Clin Oncol* 2017;**14**:611−29.
18. Magee JA, Piskounova E, Morrison SJ. Cancer stem cells: impact, heterogeneity, and uncertainty. *Cancer Cell* 2012;**21**:283−96.
19. Duan HX, Liu YH, Gao ZG, Huang W. Recent advances in drug delivery systems for targeting cancer stem cells. *Acta Pharm Sin B* 2021;**11**:55−70.
20. Bai X, Ni J, Beretov J, Graham P, Li Y. Cancer stem cell in breast cancer therapeutic resistance. *Cancer Treat Rev* 2018;**69**:152−63.
21. Keklikoglou I, Cianciaruso C, Guc E, Squadrito ML, Spring LM, Tazzyman S, et al. Chemotherapy elicits pro-metastatic extracellular vesicles in breast cancer models. *Nat Cell Biol* 2019;**21**:190−202.
22. Shackleton M, Quintana E, Fearon ER, Morrison SJ. Heterogeneity in cancer: cancer stem cells *versus* clonal evolution. *Cell* 2009;**138**:822−9.
23. Karagiannis GS, Pastoriza JM, Wang Y, Harney AS, Entenberg D, Pignatelli J, et al. Neoadjuvant chemotherapy induces breast cancer metastasis through a TMEM-mediated mechanism. *Sci Transl Med* 2017;**9**:0026.
24. Piccirillo SG, Reynolds BA, Zanetti N, Lamorte G, Binda E, Broggi G, et al. Bone morphogenetic proteins inhibit the tumorigenic potential of human brain tumour-initiating cells. *Nature* 2006;**444**:761−5.
25. Yoldi G, Pellegrini P, Trinidad EM, Cordero A, Gomez-Miragaya J, Serra-Musach J, et al. RANK signaling blockade reduces breast cancer recurrence by inducing tumor cell differentiation. *Cancer Res* 2016;**76**:5857−69.
26. Shimokawa M, Ohta Y, Nishikori S, Matano M, Takano A, Fujii M, et al. Visualization and targeting of LGR5(+) human colon cancer stem cells. *Nature* 2017;**545**:187−92.
27. Ginestier C, Wicinski J, Cervera N, Monville F, Finetti P, Bertucci F, et al. Retinoid signaling regulates breast cancer stem cell differentiation. *Cell Cycle* 2009;**8**:3297−302.

28. Li RJ, Ying X, Zhang Y, Ju RJ, Wang XX, Yao HJ, et al. All-*trans* retinoic acid stealth liposomes prevent the relapse of breast cancer arising from the cancer stem cells. *J Contr Release* 2011;**149**:281−91.
29. Gupta PB, Fillmore CM, Jiang G, Shapira SD, Tao K, Kuperwasser C, et al. Stochastic state transitions give rise to phenotypic equilibrium in populations of cancer cells. *Cell* 2011;**146**:633−44.
30. Sun T, Zhang G, Ning T, Chen Q, Chu Y, Luo Y, et al. A versatile theranostic platform for colorectal cancer peritoneal metastases: real-time tumor-tracking and photothermal-enhanced chemotherapy. *Adv Sci* 2021;**8**:2102256.
31. Deng L, Feng Z, Deng H, Jiang Y, Song K, Shi Y, et al. Rational design of nanoparticles to overcome poor tumor penetration and hypoxia-induced chemotherapy resistance: combination of optimizing size and self-inducing high level of reactive oxygen species. *ACS Appl Mater Interfaces* 2019;**11**:31743−54.
32. Deng J, Liu F, Wang L, An Y, Gao M, Wang Z, et al. Hypoxia- and singlet oxygen-responsive chemo-photodynamic micelles featured with glutathione depletion and aldehyde production. *Biomater Sci* 2018;**7**:429−41.
33. Li S, Wang Q, Shen Y, Hassan M, Shen J, Jiang W, et al. Pseudoneutrophil cytokine sponges disrupt myeloid expansion and tumor trafficking to improve cancer immunotherapy. *Nano Lett* 2020;**20**:242−51.
34. Kang T, Zhu Q, Wei D, Feng J, Yao J, Jiang T, et al. Nanoparticles coated with neutrophil membranes can effectively treat cancer metastasis. *ACS Nano* 2017;**11**:1397−411.
35. Xue J, Zhao Z, Zhang L, Xue L, Shen S, Wen Y, et al. Neutrophil-mediated anticancer drug delivery for suppression of postoperative malignant glioma recurrence. *Nat Nanotechnol* 2017;**12**:692−700.
36. Sun YX, Zhao DY, Wang G, Wang Y, Gao LL, Sun J, et al. Recent progress of hypoxia-modulated multifunctional nanomedicines to enhance photodynamic therapy: opportunities, challenges, and future development. *Acta Pharm Sin B* 2020;**10**:1382−96.
37. Overgaard J. Clinical evaluation of nitroimidazoles as modifiers of hypoxia in solid tumors. *Oncol Res* 1994;**6**:509−18.
38. Guo X, Liu F, Deng J, Dai P, Qin Y, Li Z, et al. Electron-accepting micelles deplete reduced nicotinamide adenine dinucleotide phosphate and impair two antioxidant cascades for ferroptosis-induced tumor eradication. *ACS Nano* 2020;**14**:14715−30.
39. Li X, Wei Y, Wu Y, Yin L. Hypoxia-induced pro-protein therapy assisted by a self-catalyzed nanozymogen. *Angew Chem Int Ed Engl* 2020;**59**:22544−53.
40. Chen W, Allen SG, Qian W, Peng Z, Han S, Li X, et al. Biophysical phenotyping and modulation of ALDH+ inflammatory breast cancer stem-like cells. *Small* 2019;**15**:1802891.
41. Sun R, Liu Y, Li SY, Shen S, Du XJ, Xu CF, et al. Co-delivery of all-trans-retinoic acid and doxorubicin for cancer therapy with synergistic inhibition of cancer stem cells. *Biomaterials* 2015;**37**:405−14.
42. Wei S, Kozono S, Kats L, Nechama M, Li W, Guarnerio J, et al. Active Pin 1 is a key target of all-trans retinoic acid in acute promyelocytic leukemia and breast cancer. *Nat Med* 2015;**21**:457−66.
43. Rustighi A, Zannini A, Tiberi L, Sommaggio R, Piazza S, Sorrentino G, et al. Prolyl-isomerase Pin 1 controls normal and cancer stem cells of the breast. *EMBO Mol Med* 2014;**6**:99−119.
44. Wei YH, Sun YP, Wei JJ, Qiu XY, Meng FH, Gert S, et al. Selective transferrin coating as a facile strategy to fabricate BBB-permeable and targeted vesicles for potent RNAi therapy of brain metastatic breast cancer *in vivo*. *J Contr Release* 2021;**337**:521−9.
45. Ni J, Miao TT, Su M, Naveed UK, Ju XF, Chen HY, et al. PSMA-targeted nanoparticles for specific penetration of blood−brain tumor barrier and combined therapy of brain metastases. *J Contr Release* 2021;**329**:934−47.
46. Naveed UK, Ni J, Ju XF, Miao TT, Chen HY, Han L. Escape from abluminal LRP1-mediated clearance for boosted nanoparticle brain delivery and brain metastasis treatment. *Acta Pharm Sin B* 2021;**11**:1341−54.
47. Guo Q, Zhu QN, Miao TT, Tao J, Ju XF, Sun ZL, et al. **L**RP1-upregulated nanoparticles for efficiently conquering the blood-brain barrier and targetedly suppressing multifocal and infiltrative brain metastases. *J Contr Release* 2019;**303**:117−29.
48. Han L, Jiang C. Evolution of blood−brain barrier in brain diseases and related systemic nanoscale brain-targeting drug delivery strategies. *Acta Pharm Sin B* 2021;**11**:2306−25.